University of Groningen

Bachelor Research Project Astronomy

Survival of cold gas clouds in the Circumgalactic Medium of Milky Way-like galaxies

Author:
Thomas Fortuin
(s3144089)

Supervisors:
prof. dr. Filippo Fraternali
Andrea Afruni, PhD

July 3, 2020

Abstract

A long standing question in the evolution of galaxies is how a spiral galaxy, like our Milky Way, obtains cold gas to sustain its star formation. In the last decades, observational evidence have shown that low-redshift galaxies are surrounded by a diffusive, multi-phase gas, the so-called circumgalactic medium (CGM), that extents to large galactocentric distances and that it is likely to play a very important role in the galaxy accretion of cold gas, since it defines the transition between the central disc and the intergalactic medium (IGM). Gas clouds accreted from the IGM travel through the CGM before they fall onto the galactic disc and the efficieny of this accretion mode strongly depends on the survival of the clouds. In this work we investigate whether they can survive their infall throughout the galaxy halos and accrete onto the central galaxies.

In particular, we performed high-resolution 2D hydrodynamical simulations to explore the interactions taking place at the interface between the clouds and the hot CGM gas in order to infer their survival. We investigated the survival at different locations of the galactic halos and varying the initial mass of the cloud. We have, in particular, explored the influence of thermal conduction on the survival of the clouds.

We have found that in all our simulations, a very small part of the cold clouds evaporates into the ambient hot medium and they are therefore very likely to survive their journey through the CGM. This means that massive cold gas clouds originating from the IGM could be a viable way to accrete gas onto the star-forming discs and therefore feed their star formation.

Contents

1 Introduction **3**
- 1.1 What is the Circumgalactic medium? . . . 3
- 1.2 The phases of the CGM . . . 3
  - 1.2.1 Hot phase . . . 3
  - 1.2.2 Warm phase . . . 4
  - 1.2.3 Cold phase . . . 4
- 1.3 Gas accretion . . . 5
  - 1.3.1 Galactic fountain . . . 5
  - 1.3.2 Cosmological infall accretion . . . 5
- 1.4 Aim of this thesis . . . 7

2 Methods **8**
- 2.1 Simulations . . . 8
  - 2.1.1 Euler equations . . . 8
  - 2.1.2 Radiative cooling . . . 8
  - 2.1.3 Thermal conduction . . . 9
  - 2.1.4 Effects of cooling and thermal conduction . . . 10
- 2.2 Setup of simulations and gas profiles . . . 11
  - 2.2.1 Gravitational potential . . . 12
  - 2.2.2 Initial properties of cold and hot gas . . . 12
  - 2.2.3 Setup of the simulations . . . 16
- 2.3 Resolution . . . 16

3 Results **19**
- 3.1 External regions . . . 19
  - 3.1.1 The role of thermal conduction . . . 20
- 3.2 Internal regions . . . 22
  - 3.2.1 Low mass cloud . . . 23

4 Discussion **26**
- 4.1 Drag force . . . 26
- 4.2 Balance between thermal conduction and radiative cooling . . . 29
- 4.3 Survival of the cloud . . . 32

5 Conclusions **33**

Acknowledgements **34**

References **35**

1 Introduction

1.1 What is the Circumgalactic medium?

A star-forming galaxy can be described by a galactic disc in which stars exist together with gas and dust in the so-called interstellar medium. In the last decades, more and more evidence has been found for an additional component to this classical picture of a galaxy: the circumgalactic medium (CGM, Shull, 2014 [39]). This medium consists of a diffusive, multi-phase gas that reaches large distances all the way to the virial radius. It is estimated to contain as much mass as the galactic disc (Gatto et al., 2013 [19]; Werk et al., 2014[49]), therefore it may be a solution for *the missing baryon problem* of galaxies (McGaugh et al., 2010[30]). Since it defines the transition area between the intergalactic medium (IGM) and the galactic disc, the CGM most likely plays an important role in the evolution of galaxies. It therefore can provide an explanation for the long standing question of how a galactic disc acquires gas to feed its star-formation (Crighton et al., 2013 [13]).

1.2 The phases of the CGM

The CGM is a multi-phase medium that can be divided into different phases according to its temperature:

- **Hot phase**: gas with temperatures $T \geq 10^6$ K;
- **Warm phase**: gas with temperatures $10^5 \leq T < 10^6$ K;
- **Cold phase**: gas with temperatures $T < 10^5$ K.

1.2.1 Hot phase

The hot phase of the CGM, usually called 'corona', is predicted by galaxy fountain models (White and Frenk, 1991[50]). In our Milky Way, Spitzer (1956[40]) predicted the existence of a hot halo surrounding the galactic disc in order to provide the pressure confinement for the High Velocity Clouds (HVCs, see Section 1.2.3). This hot and diffusive phase of the CGM is expected to extend out to the virial radius. However, due to the low density and therefore low X-ray surface brightness of the corona, the sensitivity of present-day telescopes struggle to detect this gas directly. Therefore, mostly indirect evidence for the existence of the corona have been found, as for instance the observed head-tail structures of HVCs, indicating an interaction of the HVCs with a hot medium (Putman, Saul & Mets, 2011[35]). Direct evidence is obtained through high-ionization absorption lines (OVII and OVIII) from background quasars and high-energy emission lines. Recent detections of these emission and absorption lines for our Galaxy inferred a mass of $\sim 4 \times 10^{10}$ $M_\odot$ within 250 kpc from the galactic disc (Miller & Bregman, 2015[31]), which is comparable to the mass of the stellar disc. This vast amount of gas present in the CGM makes it an interesting potential gas reservoir for the star formation in the disc.

1.2.2 Warm phase

The warm phase is observed with OVI absorption lines from the spectra of background quasars. The COS-Halos survey (Tumlinson et al., 2011[24]) detected these absorption lines more frequently around star-forming galaxies than passive galaxies, suggesting a relation between the presence of the warm phase gas and star formation or stellar feedback. In our Galaxy, the detection of these absorption lines suggests that the warm phase gas mostly resides inside the extra-planar gas region (see Section 1.2.3), along with the cold gas present in there. This, together with the fact that ionization models for these absorption lines predict a collisionally ionized origin, indicates that interactions between the hot corona and the cold clouds are most likely at the heart of the existence of this warm phase (Sembach et al., 2003[38]).

1.2.3 Cold phase

The cold phase is found in two types: *neutral gas* and *ionized gas*. The neutral gas resides in a layer of $\sim$ 10 kpc around the galactic disc and is called the extra-planar layer of cold gas (Sancisi et al., 2008[37]). It is observed through the neutral hydrogen 21-cm emission line and shows a peculiar kinematics: slow rotation and inflow motions. Fraternali & Binney (2008[17]) found that this neutral cold gas could be produced by the galactic fountain mechanism (see Section 1.3.1) and that it accounts for gas accretion onto the galactic disc.

In the Milky Way, a fraction of the extra-planar gas is in the form of High Velocity Clouds (HVCs, Wakker & van Woerden, 1997[47]; Marasco et al., 2011[27]). The 21-cm emission line coming from these clouds show that their velocity deviates more than $\sim$ 90 km s^{-1} from that of the galactic disc rotation (Wakker, 1991[46]). Typical HVCs are found to be within 10 kpc from the disc, using distance estimates obtained through the analysis of absorption lines in the spectra of halo stars (Wakker et al., 2007[48]). They are observed to be metal-poor (Wakker et al., 2001[45]), therefore suggesting an extragalactic origin. However, their absence in outer regions of the CGM may indicate other origins. Fraternali et al. (2015[27]) were able to prove the scenario in which extra-planar gas, and to some extent the HVCs, could originate from inside the disc with the galactic fountain, and also accrete halo gas on the galactic disc.

The cold ionized gas has been more recently discovered and there is much debate over its origin (e.g. Maller and Bullock, 2004[26]; Binney et al., 2009[8]). Due to its very low densities, it is hard to observe this gas in emission and most of the observations that we have are obtained in absorption, using the hydrogen and low-ionization metal lines (i.e. SiII, SiIII, CII, CIII, OI MgII) in the spectra of background quasars.

Different groups (Werk et al., 2012[34]; Borthakur et al., 2015[20]; Keeney et al., 2017[22]; Zahedy et al., 2019[51]) have revealed, through the analysis of these absorption lines, that all galaxies must be surrounded by a cold ionized gas component up to distances comparable to the galaxy virial radius, both around star-forming and early-type galaxies (e.g. Thom et al., 2012[43]). The

kinematics inferred for this medium reveals that this gas is composed by different clouds, bound to the central galaxy, showing a complex kinematic pattern. The analysis of the survival of these clouds will be the main focus of this thesis. Although with big uncertainty, the mass contained in the cold neutral and ionized gas together is estimated to be larger than 10^9 $M_\odot$ within 150 kpc distance from the galactic disc (Werk et al., 2014[49]). This vast amount of mass may be an potential source for gas accretion in star forming galaxies.

1.3 Gas accretion

A long standing question for the evolution of galaxies is how spiral galaxy, like our Milky Way, obtains cold gas in order to sustain its star formation. The rate in which nearby spiral galaxies have produce stars is more or less constant during their lifetimes (Aumer & Binney, 2009[7]). Typically, the star forming disc contains the amount of gas to sustain the star forming process for only a few gigayears (Kennicutt, 1983[23]). This means that a galaxy has to accrete an amount of ~ 1 $M_\odot$ yr^{-1} (Sancisi et al., 2008). Also, this gas has to be metal-poor in order to describe the observed metallicity gradient (Fraternali and Pezzulli, 2016). The question remains how a galaxy acquires this gas.

1.3.1 Galactic fountain

A possible candidate to explain gas accretion in galaxies is the galactic fountain framework (Fraternali and Binney, 2008[17]). This process is driven by stellar feedback: gas from the disc is ejected into the CGM by supernova explosions or stellar winds that creates a circulation of gas clouds from the disc to the lower CGM and then back on the galactic disc, following the motion seen in Figure 1.

During their journey through the CGM, the cold-gas galactic clouds strongly interact with the hot phase of the CGM, the corona. What happens during these interactions has been explored in different theoretical works (e.g. Marinacci et al., 2011[29]; Armillotta et al., 2016[3]). At the interface between the cloud and the corona, due to the relative motion of the two gasses, cold gas from the cloud gets stripped and mixes with the coronal gas due to Kelvin-Helmholtz instabilities. When the two gas phases mix with each other, gas at intermediate temperature starts to form (warm phase, Section 1.2.2). This decreases the cooling timescale of the hot gas, therefore making radiative cooling efficient and leading to the process of gas condensation: hot corona gas is cooled and is accreted to the fountain clouds, which means that the clouds are growing in mass. When the fountain clouds eventually fall back onto the galactic disc, they have accreted gas mass from the hot CGM that can be used for star formation.

1.3.2 Cosmological infall accretion

In current cosmological ΛCDM models, the Milky Way is expected today to accrete gas from the intergalactic medium (IGM) by hot mode accretion (Birn-

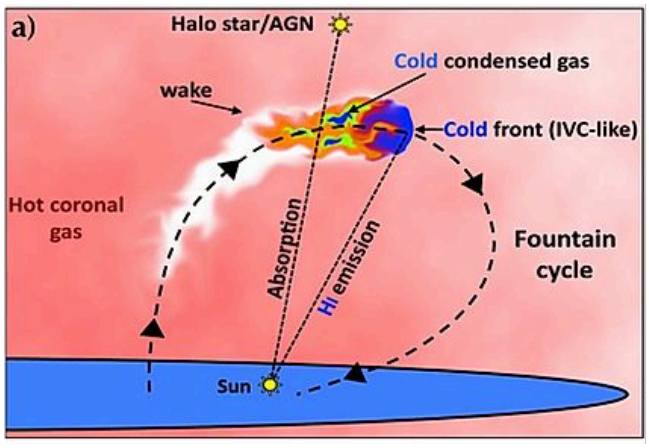

Figure 1: Schematic presentation of the fountain accretion cycle. This framework can observationally be tested. Looking at the wake behind the cloud, one will observe absorption lines of the warm gas (see section 1.2.2) from a background source. From the head of the cloud, we observe hydrogen emission lines. from Fraternali, 2017[18]

boim and Dekel, 2003[10]), where the accreting external cold gas is shock-heated to the galaxy virial temperature and is later cooling and progressively accreting towards the central galaxy. The efficiency of this process strongly depends on the length of the cooling time of the hot gas. However, hydrodynamic simulations also show that the dense parts of the infalling cold filaments could survive the journey through the hot corona of the CGM and directly reach the disc (Fernandez, Joung & Putman, 2012[34]; Joung et al., 2012[21]). The reason why these cold flows are not observed with HI emission may be due to the fact that the current generation telescopes do not have enough sensitivity to detect this emission. The large amount of cold CGM observed in the last few decades at very large galactocentric distances (see Section 1.2.3), might account for these predictions of cold gas residing in the galactic halo.

In such a cosmological infall model, the efficiency of this accretion mode strongly depends on the survival of the clouds. Armillotta et al. (2017) explored with high-resolution hydrodynamical simulations the interactions taking place at the cloud-corona interface. In Figure 2 the temprature and density snapshots of these simulations are shown. We can note how massive enough clouds can survive in the hot halo for hundreds of Myr, implying that these cold CGM clouds could be a viable way to accrete gas onto the central galaxy. In this work we will further investigate this scenario.

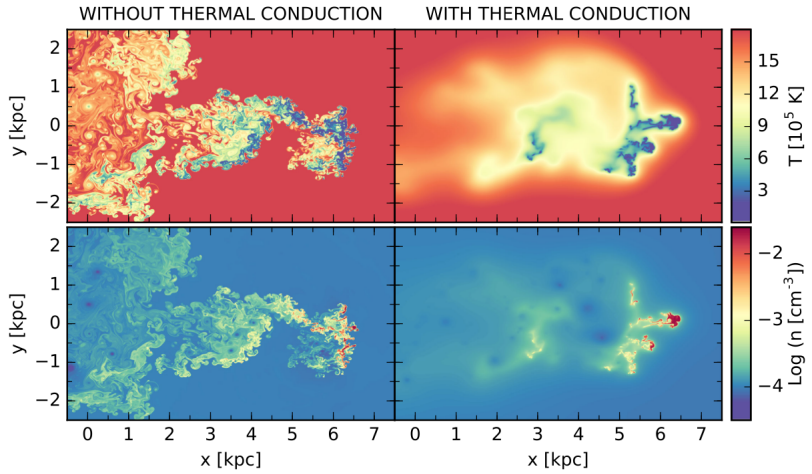

Figure 2: Temperature (top panels) and number density (bottom panels) of a simulation with initial cloud velocity of 100 km s^{-1}, inital cloud radius of 250 pc and a mass of $m_{cl} = 2 \times 10^4$ $M_\odot$ without (left panels) and with (right panels) thermal conduction. These snapshots have been taken at 200 Myr. From Armillotta et al., 2017

.

1.4 Aim of this thesis

In this work, we explore the infall model as a possible accretion mode for a Milky Way-like galaxy. We consider gas clouds coming from the IGM traveling through the hot coronal gas. We have conducted 2D hydrodynamical simulations of infalling clouds placed in the internal and external regions of the galaxy halos and investigated the influence that the interactions with the hot CGM have on the survival of the clouds. We have also explored the influence of thermal conduction in this process.

In Section 2, we present the model of our galaxy and its CGM, and introduce the hydrodynamical code that we have used for our simulations. In Section 3, we present the results of our simulations and address different physical processes at work during the cloud-corona interaction. In Section 4 we discuss our findings and we draw our conclusions about the survival of the clouds in Section 5.

2 Methods

The aim of this thesis is to analyse the cold CGM clouds in the halos of Milky Way-like galaxies and their interaction with the hot corona, using hydrodynamical simulations. In this chapter, we describe the methods used throughout the thesis. In Section 2.1, we describe the hydrodynamical code we have used to carry out our simulations. In Section 2.2, we present the way we calculated the initial properties of the cloud and the corona. In Section 2.3, we look at the influence of the resolution of our simulations on the results.

2.1 Simulations

In this section, we will introduce the hydrodynamical code we have used to perform our simulations and we will describe how the physical processes important for our investigation are implemented in the code.

We made use of the hydrodynamical code ATHENA to perform our simulations (Stone et al., 2008[41]). This is a grid-based, parallel and multidimensional hydrodynamic code that uses high-order Godunov methods to integrate numerically the Euler equations. In the past years, some advanced modifications of the code have been made to optimize it for the astrophysical purposes we are interested in. We will briefly explain the modifications here, but for a full description see the work of Armillotta et al. (2016, 2017).

2.1.1 Euler equations

The Euler equations describe the dynamics of astrophysical gases and consist of 3 conservation laws (conservation of mass, momentum and energy, respectively):

$$\frac{\partial \rho}{\partial t} + \nabla \cdot (\rho \mathbf{v}) = 0, \tag{1}$$

$$\frac{\partial \rho \mathbf{v}}{\partial t} + \nabla \cdot (\rho \mathbf{v}^2 + \mathbf{P}) = 0, \tag{2}$$

$$\frac{\partial \epsilon}{\partial t} + \nabla \cdot [(\epsilon + P)\mathbf{v}] = 0, \tag{3}$$

where ρ is the mass density, $\mathbf{v}$ is the velocity vector, $\mathbf{P}$ is a diagonal tensor with components equal to the gas pressure P and ϵ the total gas energy per unit volume. The ATHENA code integrates these functions over all the grid cells in a 3D grid over a time-step Δt and the finite-volume of each grid cell. The maximum stable allowed time-step is fixed by the Courant-Friedrics-Lewy condition (Stone et al., 2008[41]). In our case, we perform the simulations over a 2D grid instead of 3D.

2.1.2 Radiative cooling

A key process included in our simulations is radiative cooling. In general, this is taken into account as a source term in the energy equation (eq. 3), leading to

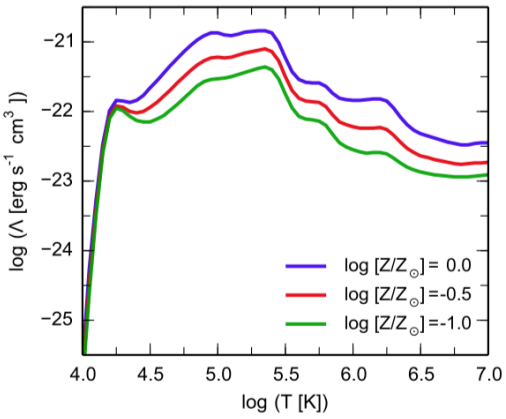

Figure 3: Cooling fuctions with different metal contents. The curves are normalized to a hydrogen number density of $n_H = 1$ cm^{-3}. The metallicity is indicated in solar units. from Sutherland & Dopita, 1993[42]

an additional term for radiative cooling. The energy equation becomes:

$$\frac{\partial \epsilon}{\partial t} + \nabla \cdot [(\epsilon + P)\mathbf{v}] = -\rho^2 \Lambda_{net}(T, Z, n_H), \tag{4}$$

where the additional term for radiative cooling/heating, $\rho^2 \Lambda_{net}(T, Z, n_H)$, is the amount of energy lost per unit volume [erg cm^{-3} s^{-1}] due to radiative cooling and heating, with $\Lambda_{net} \equiv \Lambda - H$, where Λ and H are the cooling and heating rates respectively. For simplicity, we assume that the gas in our environment is not exposed to ionizing photons, therefore assuming collisional ionization equilibrium and H=0. We use the cooling functions from Sutherland & Dopita (1993 [42]), shown in Figure 3. The cooling rate depends on metalicity Z and temprature T, $\Lambda(Z, T)$, for gas above 10^4 K, below which the cooling rate is set to zero. The algorithm makes use of a lookup table to find the cooling rate Λ.

2.1.3 Thermal conduction

An important part of this investigation is to measure the influence of thermal conduction on the survival of the clouds. The process of thermal conduction is, as with the case for radiative cooling, introduced in the Euler energy equation as a source term and results in an additional term as follows (eq. 3):

$$\frac{\partial \epsilon}{\partial t} + \nabla \cdot [(\epsilon + P)\mathbf{v}] = -\rho^2 \Lambda_{net}(T, Z, n_H) - \nabla \cdot \mathbf{q}, \tag{5}$$

where $\mathbf{q}$ is the heat conduction flux. Thermal conduction allows two different phases of gas, when in contact, to transfer heat from the hot phase to the cold

phase. This heat transfer takes place when fast moving particles from the hot phase collide with the slow moving particles in the colder phase, and transfer energy during this collision. This results in a more widespread temperature and density gradient, and influences the mixing of the two gases.

In the classical theory (Spitzer, 1962[14]), electrons conduct heat by transferring energy to other particles via collisions. This creates a heat flow $\mathbf{q}$, which is described by the heat flowing through a unit of area per unit of time and assumes an isotropic motion of electrons given as:

$$\mathbf{q} = -\kappa_{sp} \cdot \nabla T, \tag{6}$$

where κ_{sp} is the Spitzer heat conduction coefficient:

$$\kappa_{sp} = \frac{1.84 \times 10^{-5} T^{5/2}}{\ln \Psi} \text{ erg s}^{-1} \text{ K}^{-1} \text{ cm}^{-1}, \tag{7}$$

and where $\ln \Psi$ is the Coulomb logarithm:

$$\ln \Psi = 29.7 + \ln \left[\frac{T_e / 10^6 K}{\sqrt{n_e / cm^{-3}}} \right], \tag{8}$$

with n_e and T_e being the electron density and temperature, respectively.

However, this assumption of an isotropic motion of electrons breaks down in the astrophysical cases because of two reasons. First, the presence of magnetic fields forces an anisotropic motion of electrons, reducing their efficiency to conduct heat. And secondly, when the local temperature gradient is below the mean free path of the electrons, the so-called saturated regime materialises, which also decreases the efficiency of heat conduction. These two effects are taken into account in the modified code according to the following equation:

$$\mathbf{q} = -f \frac{\kappa_{sp}}{1 + \sigma} \nabla T, \tag{9}$$

where f describes the suppression due to magnetic fields and σ the ratio between classical heat flux and saturated heat flux. Throughout the thesis, we take $f = 0.1$, since the presence of a tangled magnetic field is expected to suppress the coefficient of thermal conduction by a factor ~ 10 from the Spitzer coefficient (Rechester & Rosenbluth, 1978[36]).

2.1.4 Effects of cooling and thermal conduction

In this section, we investigate the effects of the different physical processes described in the previous sections on our simulations.

Figure 4 shows the temperature distribution on our grid for a cloud starting at 100 kpc from the disc (see next Section) with an initial mass of $m_{cl} = 5 \times 10^4$ $M_\odot$ and a velocity of 100 km s^{-1} after t=20, 50, 80 Myr without cooling (left panels), with radiative cooling (middle panels) and with thermal conduction and cooling (right panels). Due to the drag force exerted by the ram pressure

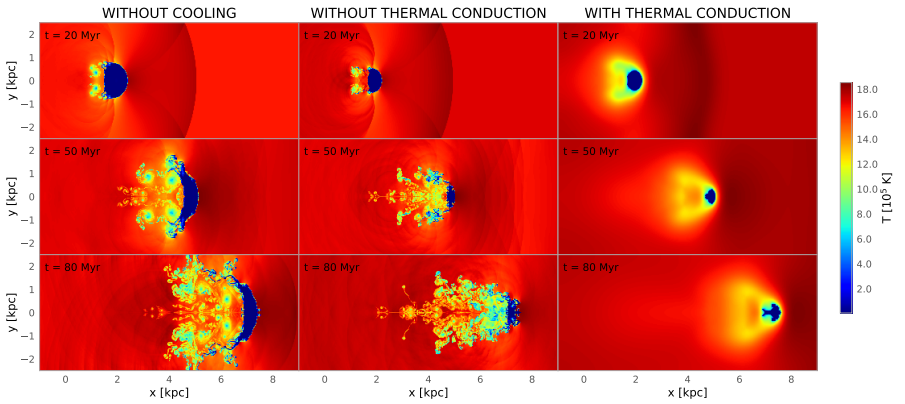

Figure 4: Temperature snapshots at 20, 50 and 80 Myr for a simulation of a moving cold cloud with mass m_{cl}=5×10$^4 M_\odot$ with a resolution of 4 pc. *Left column*: without cooling and thermal conduction; *middle column*: with only cooling; *right column:* with both cooling and thermal conduction.

of the corona, the cloud decelerates and cold gas is stripped from the cloud. Also, the relative motion between the cloud and the corona creates a shear flow over the leading face of the cloud, triggering the formation of Kelvin-Helmholtz instabilities, which allow both gas phases to mix with each other and therefore create a turbulent wake behind the cloud. In the case with and without cooling (left and middle panel), the initial spherical configuration of the cloud is heavily affected, stripping cold mass from the cloud in the form of small cloudlets which results in high temperature gradients in the wake. Note, however, the difference in the evolution of the turbulent wake between both cases: without cooling, the wake is more laterally extended, where in the cooling case it is more elongated.

In the case with thermal conduction (right panel), the initial configuration stays partially intact throughout the simulation. As explained earlier, thermal conduction is a diffusive process which therefore smooths the temperature and density gradients between the cloud and the corona. This results in a more widespread gradient and therefore hinders the development of Kelvin-Helmholtz instabilities and stripping mass from the cloud. Thermal conduction also makes the cloud more compact. Moreover, thermal conduction clearly changes the evolution of the wake with respect to the previous cases, allowing the existence of a warmer wake. We will discuss these effects in more detail in Section 3.1.1.

2.2 Setup of simulations and gas profiles

In order to define the setup of our simulations, we need to calculate the initial properties of the Milky Way-like hot circumgalactic medium. In this section we describe the treatment used to calculate these properties.

2.2.1 Gravitational potential

We assume the coronal gas to be in hydrostatic equilibrium with the galactic halo. To find the properties of the CGM, we therefore have to choose a galactic potential. We do this by first finding the virial mass and radius of the dark-matter halo. We consider a galaxy with stellar mass $\mathrm{M}_\star = 10^{10.7}$ $\mathrm{M}_\odot$. Using the stellar-to-halo mass relation described in Posti et al. (2019[33]), we calculate the virial mass of the galaxy as $\mathrm{M}_{vir} = 10^{12.3}$ $\mathrm{M}_\odot$.

The virial radius is then found as,

$$r_{vir} = \left(\frac{3M_{vir}}{4\pi \triangle_{vir} \rho_{crit}} \right)^{1/3} = 340 \text{ kpc}, \tag{10}$$

where the overdensity $\triangle_{vir}$ is calculated using the prescription in Bryan & Norman (1998[12]) at $z = 0$ and the critical density is $\rho_{crit} = 8.5 \times 10^{-27}$ kg m^{-3}.

In order to obtain the virial temperature we use (Afruni et al., 2019 [1]):

$$T_{vir} = \frac{\mu m_p G M_{vir}}{2 k_B r_{vir}}, \tag{11}$$

where $\mu = 0.6$, G is the gravitational constant, m_p is the mass of a proton and k_B is the Kevin-Boltzmann constant.

We assume that the CGM is described by a Navarro-Frenk-White profile (NFW, Navarro et al., 1996[32]). The potential of this profile is given as:

$$\Phi(r) = 4\pi G \rho_0 r_s^3 \left[\ln(1 + \frac{r}{r_s}) \frac{r_s}{r} \right], \tag{12}$$

with the central density,

$$\rho_0 = \frac{M_{vir}}{4\pi r_s^3 \left[\ln(1 + (r_{vir}/r_s) - \frac{r_{vir}/r_s}{1 + r_{vir}/r_s} \right]}, \tag{13}$$

in which the scale length is given by $r_s = r_{vir}/c$ with concentration $c = 10.2$ (Dutton and Maccio, 2014[15]). The mass inside a sphere of radius r is then described, using this potential, by:

$$M(r) = 4\pi \rho_0 r_s^3 \left[\ln\left(1 + \frac{r}{r_s}\right) - \frac{r/r_s}{1 + r/r_s} \right]. \tag{14}$$

2.2.2 Initial properties of cold and hot gas

For our Milky Way-like galaxy we assume the hot CGM to be non-isothermal ($\gamma' = 1.2$). We do this is to make sure that the densities in the central regions are not too high, as would be for isothermal profiles. The temperature of the hot phase of the CGM therefore changes with galactocentric distance, according to the following profile (Binney et al., 2009[8]):

$$\frac{T_{cor}(r)}{T_0} = 1 - \frac{\gamma' - 1}{\gamma'} \frac{\mu m_p}{k_B T_0} (\Phi(r) - \Phi_0), \tag{15}$$

where $T_0 \equiv T(r_0)$, $\Phi_0 \equiv \Phi(r_0)$ and $r_0 = 10$ kpc is a reference radius. In this thesis, we assume $T_0 = 2.8T_{vir}$, which is chosen in order to have temperatures and densities in agreement with the observations (Bregman et al., 2007[11]; Gatto et al., 2013[19]). The temperature profile is shown in the first panel of igure 5. This shows that the temperature decreases with increasing distance from the center, since it is non-isothermal. The change is however relatively small, since we use a low value for the polytropic index γ'.

Once the temperature is defined, we can obtain the density profile through (Binney et al., 2009 [8]),

$$\frac{n_{e,cor}(r)}{n_{e,0}} = \frac{T(r)}{T_0}^{1/(\gamma'-1)}, \tag{16}$$

where $n_{e,0} \equiv n_e(r_0) = 3 \times 10^{-4}$ cm^{-3} is chosen in order to have a mass for the corona of 20% of the total baryonic mass inside the halo, to be consistent with observational estimates (Anderson & Bregman, 2011[2]). To obtain the number density, we assume mass abundances of $Y = 0.25$ and $X = 0.75$, which then gives us the number density of the corona as $n_{cor}(r) = 2.1 n_{e,cor}(r)$.

We then set the temperature of the clouds to $T_{cl} = 2 \times 10^4$ K, which is in agreement with observational estimates (e.g. Werk et al., 2014[49]). To find the density of the clouds, we assume that they are in pressure equilibrium with the corona (Armillotta et al., 2017 [4]). This gives us the number density for the cold gas n_{cl}, through:

$$n_{cl}(r) T_{cl} = n_{cor}(r) T_{cor}(r). \tag{17}$$

The density profiles for the hot and cold gas are shown in the second panel of Figure 5. Both densities decrease with the galactocentric radius, and the density of the cold gas is always higher than the density of the coronal gas, due to the lower temperature of the cold clouds (eq. 17).

Once the density of the cloud is obtained, we can estimate the radius of the cloud using:

$$r_{cl} = \left(\frac{3 m_{cl}}{4\pi \rho_{cl}} \right)^{1/3}, \tag{18}$$

where m_{cl} is the assumed mass of the cloud and $\rho_{cl} = \mu m_p n_{cl}$ is the density of the cloud, with $\mu = 0.6$ which is the mean molecular weight for ionized gas. The high uncertainty in the observations do not allow us to know a priori the mass of the cold CGM clouds (Werk et al., 2014). Therefore, in this work we decided to assume a cloud of mass $m_{cl} = 5 \times 10^4 M_\odot$. However, in Chapter 3 we will also consider a cloud with lower mass, in order to investigate how this influences the cloud survival. The third panel in Figure 5 shows that the radius of the cloud increases with increasing distance from the galactic center.

The last step is to find the velocity of the cloud with respect to the corona. Since we are exploring a scenario in which the cold CGM clouds are accreted from the IGM and move through the halo towards the galactic disc, the motion

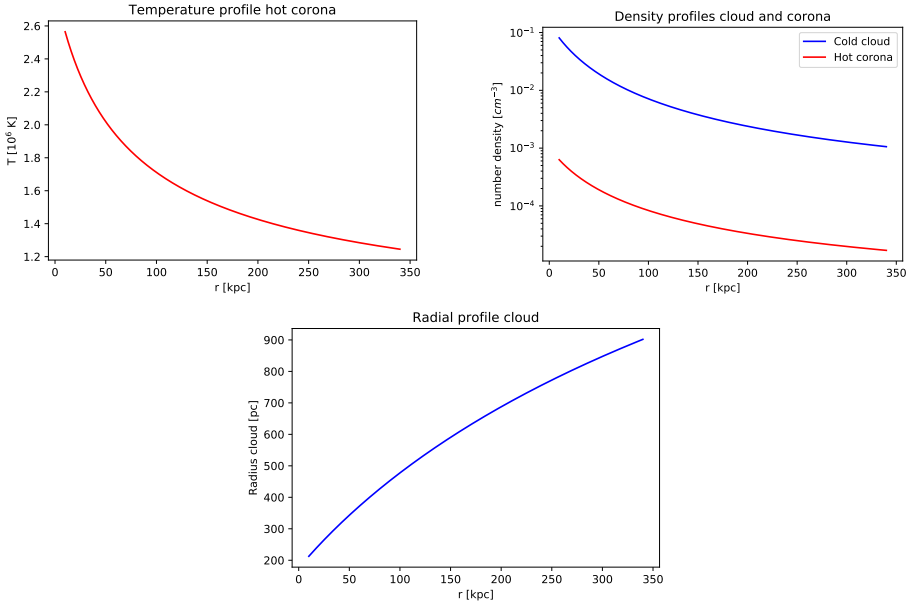

Figure 5: Profiles of the temperature of the corona (eq. 15), the density of the corona (eq. 16) and the cold clouds (17) and radius of the cold clouds (eq. 18) as a function of galactocentric radius. These profiles are calculated for our fiducial galactic halo and a cloud with mass $m_{cl} = 5 \times 10^4 M_\odot$.

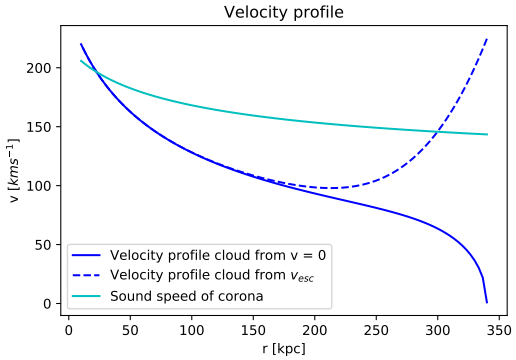

Figure 6: Velocity profiles of infalling clouds (eq. 21) starting at r_{vir} with $v_0 = 0$ (solid blue curve) and with $v_0 = v_{esc}$ (dashed blue curve). In both cases the mass of the cloud is $m_{cl} = 5 \times 10^4 M_\odot$. The sound speed of the non-isothermal corona (eq. 23) is shown in cyan.

of the cloud is determined by the gravitational force:

$$\frac{dv(r)}{dr} = \frac{1}{v_(r)} \frac{GM(r)}{r^2}, \tag{19}$$

where v is the cloud infall velocity and $M(r)$ is the mass inside the galactocentric radius r calculated by equation (14).

While the cloud is moving through the halo, it will feel a drag force exerted by the ram pressure coming from the hot coronal gas in the CGM. This will decelerate the cloud with (e.g. Marinacci et al., 2011[29]):

$$\dot{v}_{drag} = \frac{\pi r_{cl}^2 \rho_{cor} v^2}{m_{cl}}. \tag{20}$$

Taking into account both of these effects, the resulting equation of motion is then given by (Afruni et al., 2019[1]):

$$\frac{dv(r)}{dr} = \frac{1}{v(r)} \frac{GM(r)}{r^2} - \frac{\pi r_{cl}^2(r) \rho_{cor}(r) v(r)}{m_{cl}}. \tag{21}$$

In order to solve equation (21), we need to find a starting value for the velocity of the cloud at the virial radius. We will take into account two extreme cases. One in which the clouds are starting from the virial radius at rest, and the other where they start with the escape velocity at the virial radius, given by:

$$v_{esc} \equiv \sqrt{\frac{2GM_{vir}}{r_{vir}}}. \tag{22}$$

In Figure 6 we show the analytic calculated velocity profile for both scenarios. We can see that at 150 kpc from the galactic disc, the two velocity profiles

overlap with each other. This can be explained by the effect of the drag force. In equation (21), when the velocity is high, the drag force increases, which results in a higher deceleration of the cloud. Therefore the cloud starting at the escape velocity will experience a higher deceleration, until the velocity is slowed down to a value where the drag force is in equilibrium with the gravitational force that pulls the cloud towards its center.

Figure 6 also shows the sound speed of the corona:

$$c_s(r) = \sqrt{\gamma' \frac{k_B T_{cor}(r)}{\mu m_p}}, \tag{23}$$

where the polytropic index $\gamma' = 1.2$, $\mu = 0.6$ and $T_{cor}(r)$ is the temperature of the corona described by equation (15). Since the corona is non-isothermal, its sound speed varies with distance from the galactic disc. Note how the velocity predicted by equation (21) generally stays below the sound speed. Only in the most external regions, in the case of clouds starting at the virial radius with escape velocity, the cloud is supersonic as well as in the very center. However, since the escape velocity is an upper limit for the initial cloud velocity and it represents an extreme scenario, we will not explore the motion of supersonic clouds in this work.

2.2.3 Setup of the simulations

With the properties of CGM gas calculated in the section above, we will explore in Chapter 3 the behaviour of the cold clouds moving through the corona at different starting points. We consider as reference distances 100 kpc and 50 kpc from the central galaxy as external and internal regions, respectively. In the most external regions, our analytic CGM model shows a very low density of the coronal gas (Figure 5), therefore very little interaction is expected to take place. That is why we expect that this region does not have a significant impact on the survival, and we start our investigation at 100 kpc. All the simulations that we carried out in this work are listed in Table 1.

2.3 Resolution

In order to test the reliability of our simulations, we test the code for convergence. We do this to study if the resolution of the grid has a strong impact on the outcome of the simulation.

As seen in Figure 4, the turbulent wake in the case without thermal conduction consists of small cloudlets with high temperature gradients. The numerical diffusion algorithm tries to truncate these substructures by smoothing out the gradients on scales of a few times the grid resolution. Therefore the higher the resolution (i.e. smaller grid cell size), the greater the concentration of cold material in these substructures. This means that the result of a simulation without thermal conduction varies with the resolution of the grid. It is therefore extremely difficult to reach convergence between results at different resolutions in a simulation without thermal conduction (see McCourt et al., 2016[25]).

Sim.	starting from (kpc)	TC	v (km s^{-1})	m_{cl} ($M_\odot$)	n_{cor} (cm^{-3})	n_{cl} (cm^{-3})	r_{cl} (pc)	Resolution (pc x pc)
1	100	off	100	5×10^4	8.3×10^{-5}	0.007	347	4
2	100	on	100	5×10^4	8.3×10^{-5}	0.007	483	4
3	50	off	100	5×10^4	0.00019	0.019	347	4
4	50	on	100	5×10^4	0.00019	0.019	347	4
5	50	on	175	5×10^4	0.00019	0.019	347	4
6	50	off	100	1×10^4	0.00019	0.019	203	4
7	50	on	100	1×10^4	0.00019	0.019	203	4
8	50	on	100	5×10^4	0.00019	0.019	347	2
9	100	on	100	5×10^4	8.3×10^{-5}	0.007	483	2
10	30	on	100	5×10^4	0.0003	0.0350	284	4

Table 1: Overview of hydrodynamical simulations performed with ATHENA. All the simulations have been run for 80 Myr.

Thermal conduction also is a diffusive process that smooths the temperature gradient, but unlike numerical diffusion, this depends on physical conditions. When thermal conduction becomes the dominant diffusive process over numerical diffusion, increasing the resolution will have a lower impact on the outcome of the simulation (Armillotta et al., 2017[4]). It is therefore easier to reach convergence between simulations of different resolutions when thermal conduction is present.

In Figure 7 we show the evolution of cold gas mass present in the grid for a simulation with thermal conduction at different resolutions of a cloud starting at 100 kpc with initial mass $m_{cl} = 5 \times 10^4 M_\odot$ and initial velocity of 100 km s^{-1}. We are particularly interested in this quantity, since we want to investigate the cloud survival with time. We will therefore look at this cold mass evolution extensively for all our simulations in the next Chapters. To obtain this profile, we sum all the mass contained in the grid cells with cold gas ($T < 10^5$ K) and we multiply the result for $(4/3)r_{cl}$, which is a normalization factor to convert our results, which are in 2D and therefore represents the cloud as cylinder, to 3D, which represents the cloud spherically (Marinacci et al., 2010[28]). We can see that the losses seem to increase slightly by increasing the resolution. The differences between the profiles at 2 and 4 pc resolution are however small (less than 1%), meaning that we are potentially close to the convergence point and our results are valid. For the rest of this work, we will use 4 pc as our fiducial resolution.

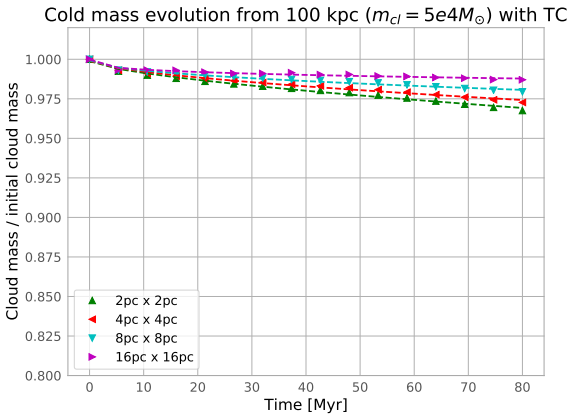

Figure 7: Cold mass evolution with different resolutions of a moving cloud with $m_{cl} = 5 \times 10^4 M_\odot$ and starting at r=100 kpc with thermal conduction active.

3 Results

In this section we present the results of the hydrodynamical simulations that we performed in this work. In Section 3.1, we show the results for a cloud moving in the external regions of the galactic halo, at a distance of 100 kpc from the galactic disc (see Chapter 2). In Section 3.2, we focus on the internal regions, at a distance of 50 kpc from the galactic disc.

3.1 External regions

We present the results of a simulation with a cloud of mass $m_{cl} = 5 \times 10^4$ $M_\odot$ starting its infall motion at a distance of 100 kpc from the galactic center, with the properties discussed in Chapter 2, both with and without thermal conduction. We follow the cloud for 80 Myr.

Figure 8 shows the temperature snapshots at 20, 50 and 80 Myr, while in Figure 9 we show the evolution of the cold gas mass ($T < 10^5$ K) and the velocity of the cloud. Although both with and without thermal conduction the cloud loses cold mass, we can distinguish different trends between the two cases. After 80 Myr, the cloud lost 2.7% of its initial mass in case of thermal conduction and 2.2% in the case when thermal conduction is absent. Therefore, in both cases the cloud is not strongly affected by the interactions with the hot gas and manages to retain most of its mass, as expected at these distances, where the

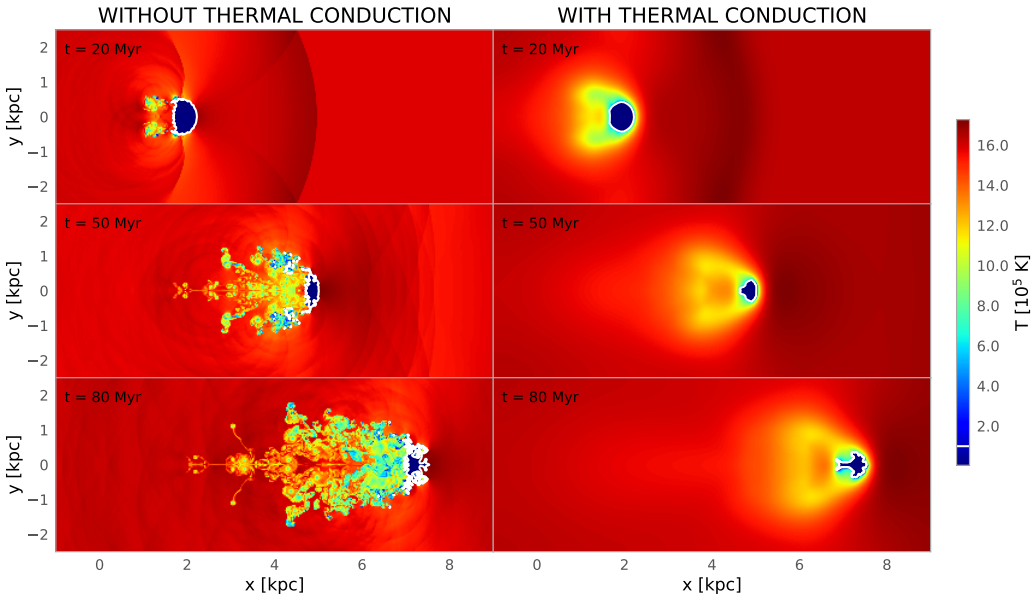

Figure 8: Temperature snapshots at 20, 50 and 80 Myr with white contours placed at $T = 10^5$ K of sim. 1 (left) and sim. 2 (right) from Table 1.

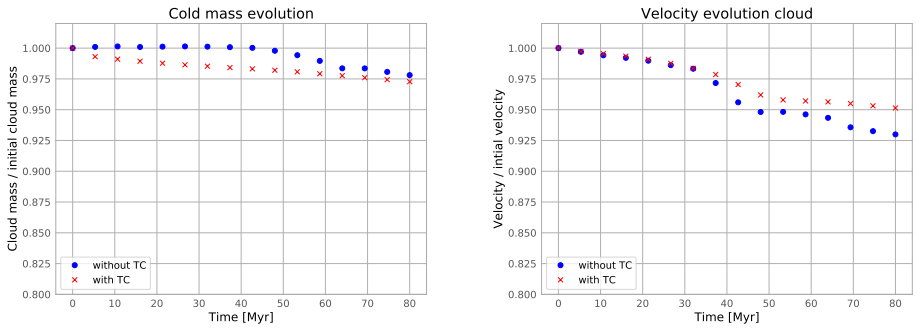

Figure 9: Results of sim. 1 (blue) and sim. 2 (red) from Table 1. Left: cold ($T < 10^5$ K) mass evolution profile; right: velocity of the cold gas.

corona has a very low density ($n_{cor} = 8.3 \times 10^{-5}$ cm^{-3}).

When looking at the evolution of the cloud velocity (see Figure 9), we see that the cloud decelerates slightly because of the interaction with the hot corona. After 80 Myr, the cloud travels at 95% of its initial velocity with thermal conduction and at 93% without thermal conduction.

3.1.1 The role of thermal conduction

In order to better understand the effect of thermal conduction on the survival of the mass of the cold cloud, we show the mass distribution as a function of temperature, with and without thermal conduction, in Figure 10. This helps us to understand how the mass is distributed among different gas phases and how this distribution changes with time. We clearly see the peaks around the typical temperatures of the cloud and the corona at the beginning of the simulation (t = 0 Myr). When the cloud is starting to move through the coronal gas, due to the mixing in the turbulent wake, the amount of mass at intermediate temperatures starts to increase.

In the case of thermal conduction, this evolution of the turbulent wake is slow: there is not much mass at intermediate temperatures in the wake. This can be explained by the dual role of thermal conduction (Armilotta et al., 2017 [5]). Thermal conduction creates a more widespread temperature gradient at the interface between the corona and the cloud, which keeps the cloud compact, as already explained in Section 2.1. However, when gas is stripped from the cloud, due to thermal conduction this cold mass evaporates extremely fast. This can be seen from the high amount of mass at high temperature ($T \simeq 10^6$ K) in Figure 10.

When looking at the mass distributions for the case without thermal conduction, the turbulent wake is much more developed (also seen from the snapshots in Figure 8). The ram pressure of the corona is able to strip much more gas from the cloud and both gas phases start to mix due to Kelvin-Helmholtz instabilities. Therefore the mass situated at intermediate temperatures is much

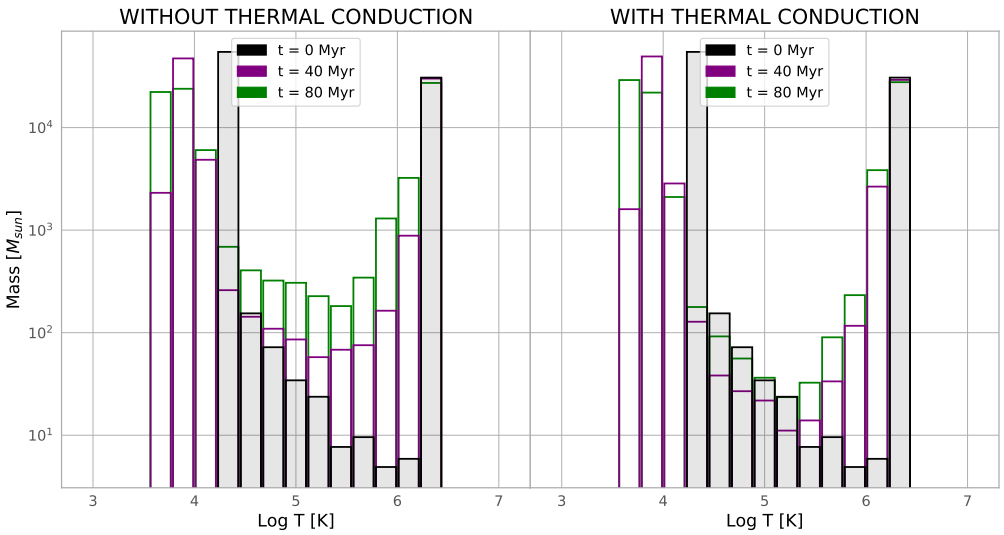

Figure 10: Mass distribution as a function of temperature at different times (t=0, 40, 80 Myr) of sim. 1 and sim. 2 from Table 1.

higher than in the case of thermal conduction, with more gas at a temperature of $T \simeq 10^5$ K. Note that this is the peak of the cooling function and therefore the cooling becomes efficient. However, at the end this effect is outbalanced by shock heating and evaporation of cold gas.

We can also see that the mass at temperatures below the initial cloud temperatures is growing, indicating that the core of the cloud is cooling.

3.2 Internal regions

In the previous section we have seen that the mass losses in the external regions are extremely small and therefore the clouds are likely to survive the journey to the inner regions of the CGM. In this section, we explore the survival of clouds at 50 kpc from the galactic disc. The properties of the CGM derived in Chapter 2 show a higher density ($n_{cor} = 8.3 \times 10^{-5}$ cm^{-3}) and temperature ($T_{cor} = 2 \times 10^6$ K) of the coronal gas at this location, therefore we expect more interactions, possibly influencing the survival of the cloud. Figure 11a shows the temperature snapshots of a cloud with mass m_{cl}=5×10^4 M$_\odot$ starting at 50 kpc from the galactic center, with a velocity of 100 km s^{-1}, with and without thermal conduction. During the simulation without thermal conduction, due to technical problems the simulation crashed after 60 Myr. The resulting profiles in Figure 12 for the cold mass and velocity evolution show that, even in the internal

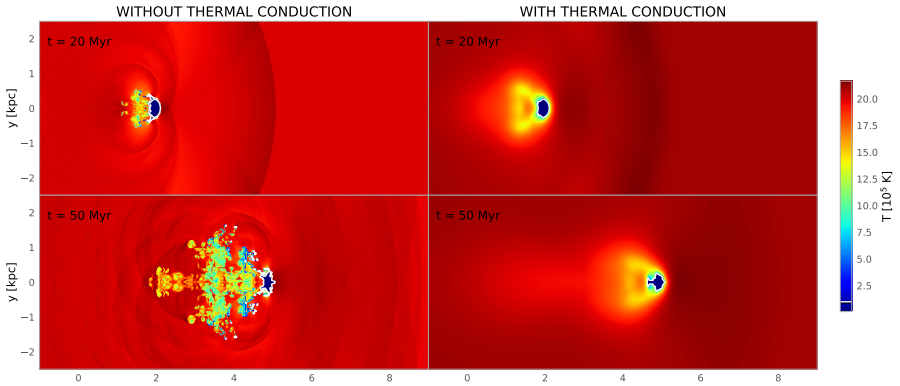

(a)

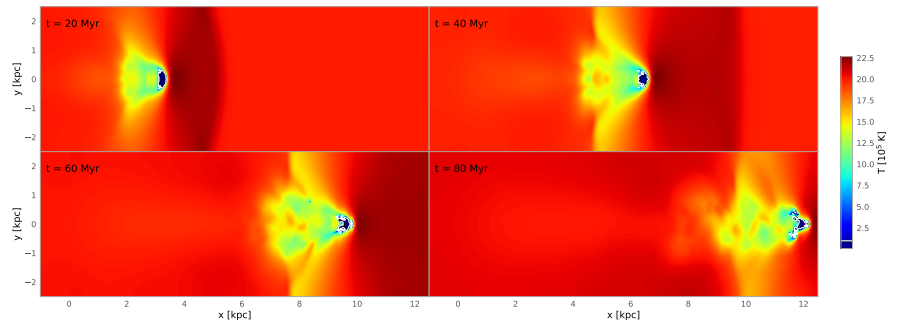

(b)

Figure 11: *a*: Temperature snapshots at at t=20, 50 Myr for sim. 3 (left) and sim. 4 (right); *b*: Temperature snapshots at t=20, 40, 60, 80 Myr for sim. 5. (see Table 1)

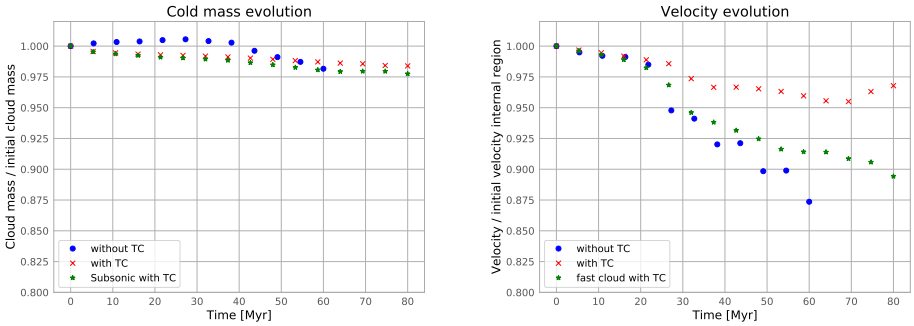

Figure 12: Results of sim. 3 (blue), sim. 4 (red) and sim 5. (green) from Table 1. Left: cold mass evolution profile; right: velocity of cold gas.

regions, after 80 and 60 Myr, the cold mass losses are extremely small: 1.6% with and 1.8% without thermal conduction (after 60 Myr). We can conclude that the cloud of mass m_{cl}=5×10$^4 M_\odot$ is able to survive also in these regions of the CGM, and we will do a more thorough analysis on the cloud survival and its analytical predictions in Section 4.2.

When looking at the velocity evolution (right panel in Figure 12), the difference between both cases becomes more apparent. Without thermal conduction, the deceleration becomes much steeper than with thermal conduction. In Section 4.1, we will look deeper into this effect.

So far we have carried out our simulations with a cloud that is moving with a velocity of 100 km s^{-1} with respect to the hot corona. We did this in order to have a good comparison of the survival of the cloud between the internal and external regions. The analytical velocity of our CGM model in Chapter 2 (Figure 6) shows that in the external regions a relative cloud velocity of 100 km s^{-1} represents the physical case reasonably well. However, in the internal regions, we see that a cloud of mass $m_{cl} = 5 \times 10^4\ M_\odot$ reaches a velocity of $\sim$ 175 km s^{-1}, which is close to the speed of sound of the hot coronal gas at that distance. Armillotta et al. (2017) [5] showed that the survival of the cloud also depends on its velocity. We therefore carried out a simulation with thermal conduction for a cloud with a velocity of 175 km s^{-1} with respect to the corona, in order to see its effect on the survival (see Figure 11b). The green profiles in Figure 12 show the evolution of cold mass and the velocity of the cloud for this simulation. From these profiles we can see that the results are comparable to the one obtained with a cloud moving at a lower velocity. Therefore it is possible that also clouds that move at slightly supersonic velocity are able to survive.

3.2.1 Low mass cloud

The results of our simulations so far have shown that the cold mass losses are extremely small in the external and internal regions for a cloud of m_{cl}=5×10^4

$M_\odot$. Armillotta et al. (2017[5]) showed that the mass losses increase with decreasing cloud mass. We therefore also ran a simulation of a cloud with mass m_{cl}=1×10^4 $M_\odot$ at 50 kpc from the galactic disc, in order to see how that changes the survival of the cloud in the hot CGM. In Figure 13 we show the temperature snapshots at 20, 50 and 80 Myr. From this figure we see that without thermal conduction, the rate of cloud destruction from its initial spherical configuration is even more than in case of the high mass cloud. This increases the mixing of cloudlets with the corona in the wake. Figure 14 shows the cold mass evolution and the cloud velocity evolution. This shows that after 80 Myr, the cloud has lost 3.4% of its mass with and 6.4% without thermal conduction. Even though these cold mass losses are bigger than in the previous cases, the losses are still not significant and therefore it is possible that also the less massive clouds will survive for a relatively long time (Section 4.3).

In Figure 15 we show the mass distribution as a function of temperature. The same pattern appears here as in Section 3.1.1 when thermal conduction is off. However, since the destruction of the low mass cloud is higher as we have already seen from the temperature snapshots, due to subsequent mixing of both gas phases, the fraction of gas at the peak of the cooling function, $T \simeq 10^5$ K, is higher, therefore allowing more hot gas to cool. This explains the ability of the cloud to retain its mass for a longer period of time, as seen from the mass profile in Figure 14. However, when this effect is outbalanced by the evaporation of cold gas, due to the complete destruction, the cold mass drops faster.

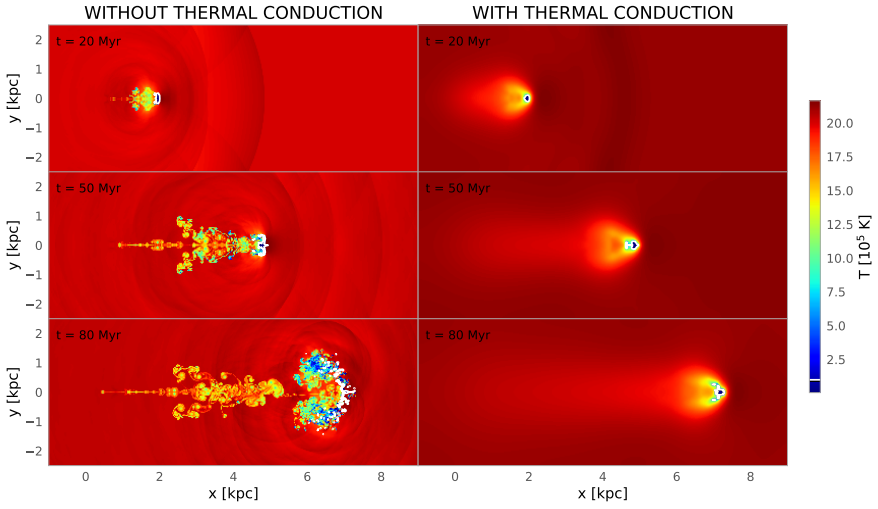

Figure 13: Same as Figure 8. Left: sim. 6; right: sim. 7.

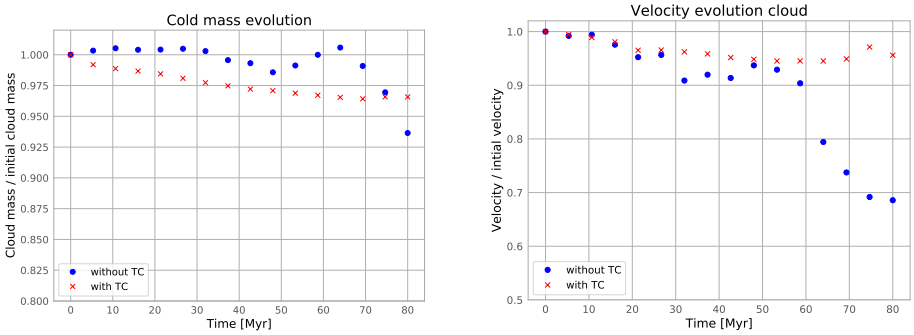

Figure 14: Results of sim. 6 (blue), sim. 7 (red) from Table 1. Left: cold mass evolution profile; right: velocity evolution of cold cloud.

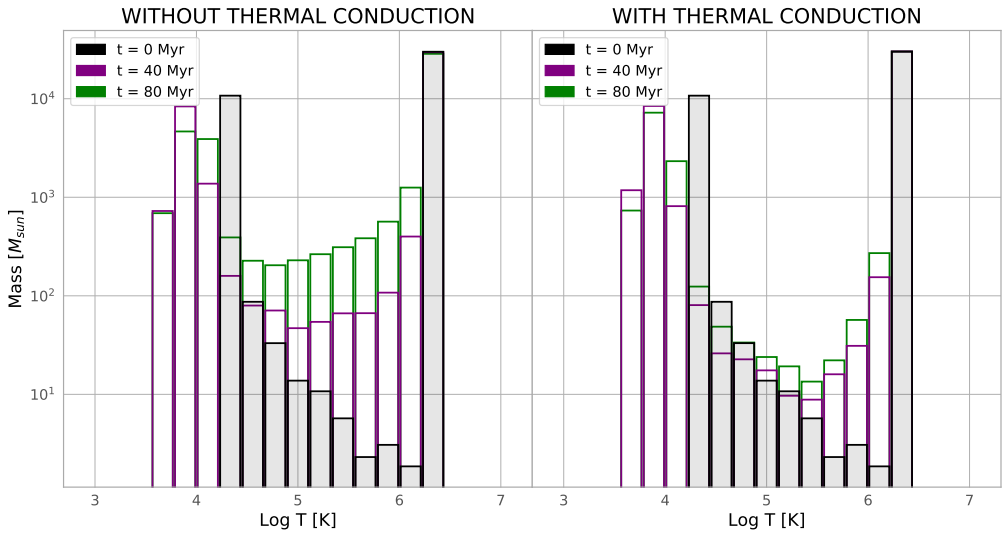

Figure 15: Mass distribution at different times (t=0, 40, 80 Myr) for sim. 6 (left) and sim. 7 (right) from Table 1.

4 Discussion

In this section, we further explore the physical processes at work in our simulations and we discuss the implications of the results obtained in Chapter 3 in the context of accretion of cold gas into a Milky Way-like galaxy. In Section 4.1, we look at the drag force. In Section 4.2, we describe the theory of the Field length in order to investigate what happens at close distances from the galactic disc. In Section 4.3 we discuss the survival of the cloud.

4.1 Drag force

The ram pressure of the corona exerts a drag force on the cloud. This drag force affects the motion of the clouds decelerating them, following the prescription of Fraternali et al. (2008[9]):

$$v_{cl}(t) = \frac{v_{cl}(0)}{1 + t/t_{drag}}, \tag{24}$$

where the timescale t_{drag} for the drag force is given as:

$$t_{drag} = \frac{m_{cl}}{v_{cl}\sigma\rho_{cor}}, \tag{25}$$

where $\sigma = \pi r_{cl}^2$ is the cross section of the cloud, m_{cl} and v_{cl} are, respectively, the mass and velocity of the cloud (with respect to the hot gas) and ρ_{cor} is the density of the hot corona. We compare the analytic velocity profile (eq. 24) with the observed velocity profiles for the external, internal and low mass cases in Figure 16. This shows that the analytic velocity profile, equation (24), overestimates the efficiency of the drag force. Also, we see the difference in the velocity profiles between with and without thermal conduction, especially in the internal regions. The differences between the two types of simulations and between the simulations and the analytic predictions are mainly due to the differences in the cross section of the cloud between the different treatments. Indeed, as we can see from equation (24) and equation (25) given the mass of the cloud, the cross section of the cloud plays an important role in the efficiency of the drag force, and consequently the deceleration of the cloud.

Looking at the temperature snapshots in the Figures 8, 11 and 13, without thermal conduction, we see the strong cloud deformations that are taking place. This increases the cross section of the clouds.

In Figure 17 we projected the distribution of cold mass on the y-axis present in the grid, for the three main simulations analysed in Chapter 3: external regions, internal regions and low mass cloud in the internal regions. The y-axis is the dimension perpendicular to the motion of the cloud, and thus the dimension on which the drag exerts a force. In particular, the width of this distribution gives us an indication of the total extention of the cloud and therefore its cross section.

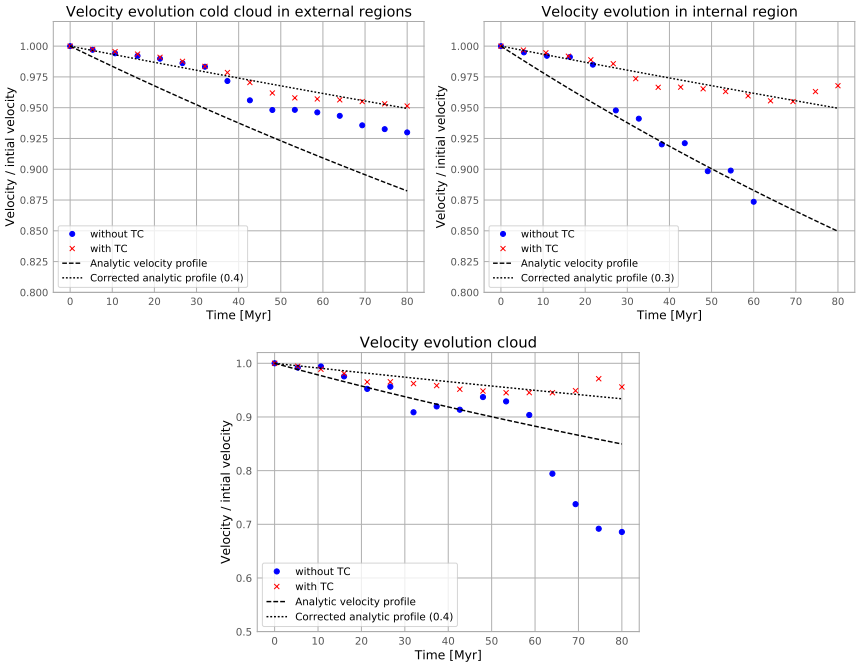

Figure 16: Velocity of the cold gas in the simulations compared with the analytic velocity profile with (dashed line) and without (dotted line) the correction factor for a high mass cloud in external regions (upper left panel), a high mass cloud in internal regions (upper right panel) and a low mass cloud in internal regions (bottom panel). Simulations are run with (red) and without (blue) thermal conduction.

The analysis of these plots confirms that thermal conduction keeps the cloud compact, and we can see how the cross section (the width of the mass distribution), decreases with time. Without thermal conduction instead, the cloud does not stay compact and we see a flattening of the cloud that results in an increase of the cross section. This effect is more evident in the internal region and for a low mass cloud.

To better understand what happens when the cross section increases, we investigated the streamlines of the gas in the simulation of a high mass cloud in the external regions in Figure 18 in which we compare with and without thermal conduction. A streamline shows, given the velocity vector, the direction in which the gas in a cell will flow in the subsequent timestep. The figure reveals in both simulations the formation of vortices behind the cloud, explaining the turbulent wake and the deformation of the cloud. This dissipates kinetic energy from the cloud and decelerates it. Without thermal conduction, the increase in cross section results in more vortices consequently dissipating more kinetic energy and decelerating the cloud. This effect is experienced strongly for a low mass cloud

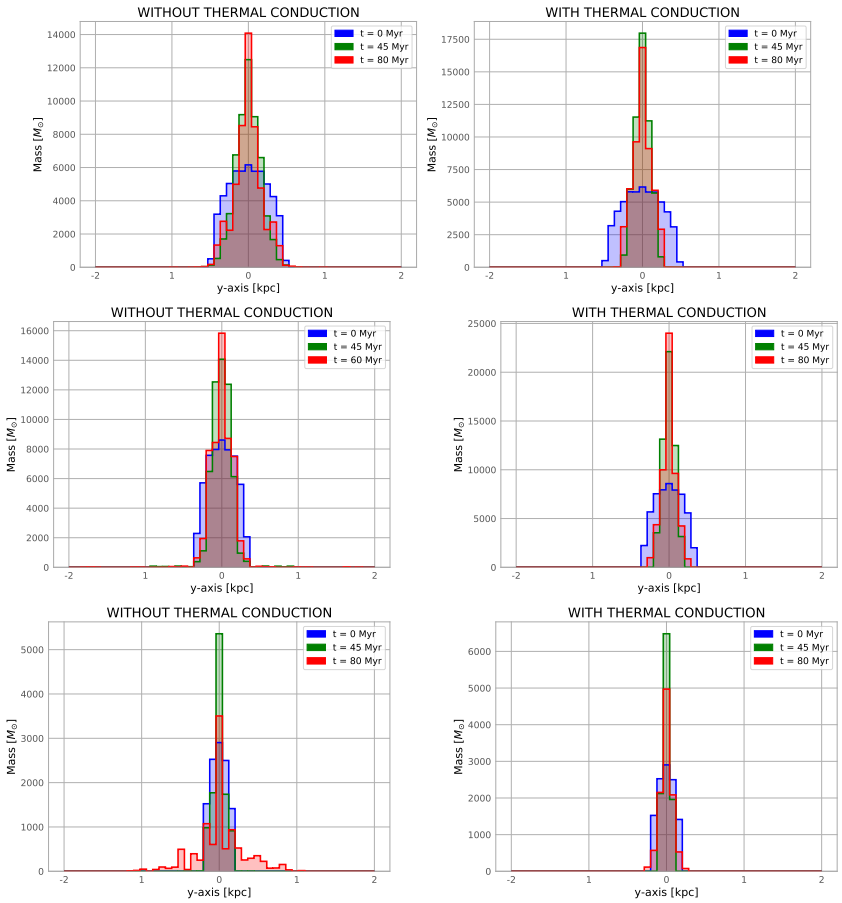

Figure 17: Projection of the mass distribution on the y-axis of the simulation grid at different time-steps (t=0, 45, 80 Myr) for a high mass cloud in external regions (top panels), a high mass cloud in internal regions (center panels) and a low mass cloud in internal regions (bottom panels): with (right panels) and without thermal conduction (left panels).

starting in the internal regions without thermal conduction, where between 40 and 65 Myr there is a sudden drop in velocity (Figure 16). In Figure 19 we show the temperature snapshots and the streamlines at 40 and 60 Myr. This shows that during that time interval the cloud deforms heavily, increasing its cross section and therefore explaining the high deceleration.

The effects described above explain the differences between the velocity profiles of the simulations with and without thermal conduction. It is therefore clear that the analytic prescription described by equation (24), valid for a spherical cloud, cannot take into account all these second-order effects observed in the simulations and therefore it is expected to deviate from our findings.

Given the previous discussion, we would expect the analytical prediction to lie above the simulated velocity profile. However, the opposite is true in most cases. This could be due to the fact that the analytic velocity profile in equation (24) treats the cloud as a sphere in three-dimensions. Our simulations are in two-dimension, therefore resulting in a lower cross section in the simulated clouds, which means that the velocity in the simulations may be overestimated. In order to overlay the analytic velocity profile with the observed profile, we made use of a correction factor for the cross section, that might take into account all these effects we just described. It appeared that this correction factor is between 0.3-0.4, therefore quite small, meaning that, with some uncertainties, the analytic prescription approximates reasonably well the motion of the clouds and their deceleration due to the drag force. We can thus consider the results of our simulations in agreement with the analytic predictions, therefore justifying the analysis of the CGM velocities in Chapter 2.

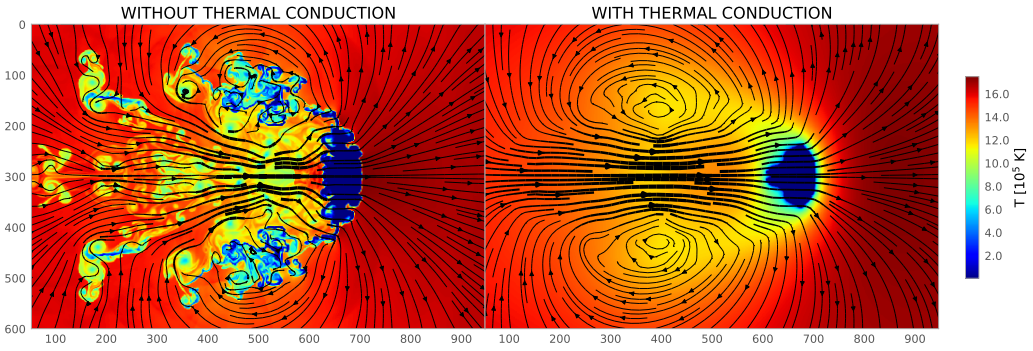

Figure 18: Streamlines present in the grid superimposed over the temperature snapshot for a high mass cloud starting in the external region with (right panel) and without (left panel) thermal conduction. The time of this is snapshot is 60 Myr. Both columns are on the same scale.

4.2 Balance between thermal conduction and radiative cooling

In the case of thermal conduction, a quantity that is interesting to analyse is the Field length, defined as (Field, 1965[16]):

$$\lambda_{field} \equiv \sqrt{\frac{f\kappa_{sp}T_{cor}}{n_{cl}^2\Lambda(T_{cl})}} \tag{26}$$

where $f = 0.1$ is the efficiency of thermal conduction (see Section 2.1.2), κ_{sp} is the Spitzer heat conduction coefficient (eq. 6), T_{cor} is the temperature of the hot corona, n_{cl} is the density of the cloud and $\Lambda(T_{cl})$ is the cooling rate of

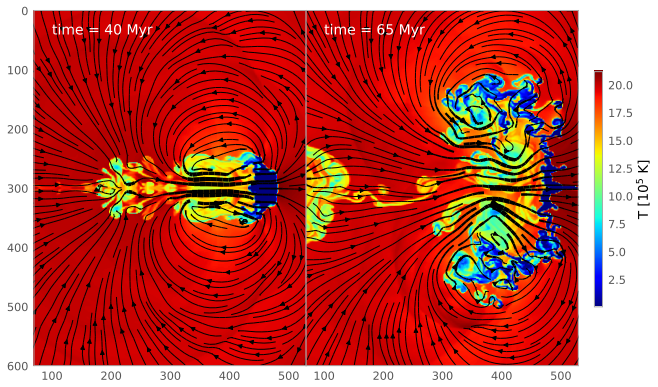

Figure 19: Streamlines present in the grid superimposed over the temperature snapshot for a low mass cloud starting in internal region without thermal conduction at $t = 40$ Myr (left column) and $t = 65$ Myr (right column). Both columns are on the same scale.

the cold gas, which we take as $10^{-23.93}$ erg cm^3 s^{-1} as the average cooling rate between the temperature range 10^4-$10^{4.3}$ K (Armillotta et al. 2016[6]).

This critical length scale can be used to investigate the evolution of a two-phase medium when in contact with each other (in our case the cloud and the hot corona). It can be used to estimate whether heat transfer (i.e. thermal conduction evaporating cold gas) or radiative cooling (which means gas condensation: hot corona gas is cooled) is more efficient over the other. When the length scale l of the structure (i.e. the cloud) is greater than the the field length ($l > \lambda_{field}$), radiative cooling is dominant and the cloud will grow cold mass, otherwise thermal conduction dominates and the cloud will evaporate into hot gas.

In Figure 20 we show the Field length (eq. 26) as a function of the distance from the galactic center and we compare it with the radius of the cloud. Note how at large distances, the Field length exceeds the scale length of the cloud and we thus observe a regime where the influence of thermal conduction dominates over radiative cooling, as we have found in our simulations. Around ~ 40 kpc, there is a change in regime, below which radiative cooling dominates. To see if this is happening, we ran a simulation starting at 30 kpc to see if the cloud is growing cold mass (Figure 21). Figure 22 shows the cold mass evolution for this simulation. After 80 Myr, the mass of the cloud has increased by 0.4% which is a small fraction but it clearly indicates the cloud is not losing mass and therefore is able to survive the central regions of the CGM, which is in agreement with what was found in Armillotta et al. 2016[6].

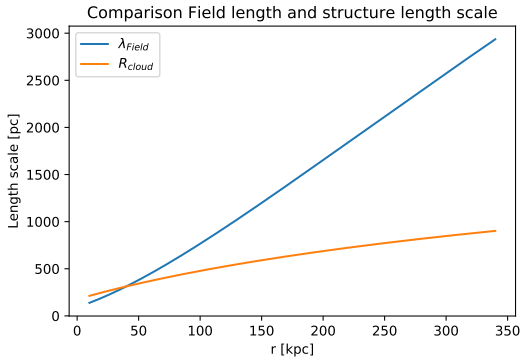

Figure 20: Comparison between Field length (eq.26) and radius (eq.18) for a cloud with $m_{cl} = 5 \times 10^4 M_\odot$ as a function of distance to the galactic center.

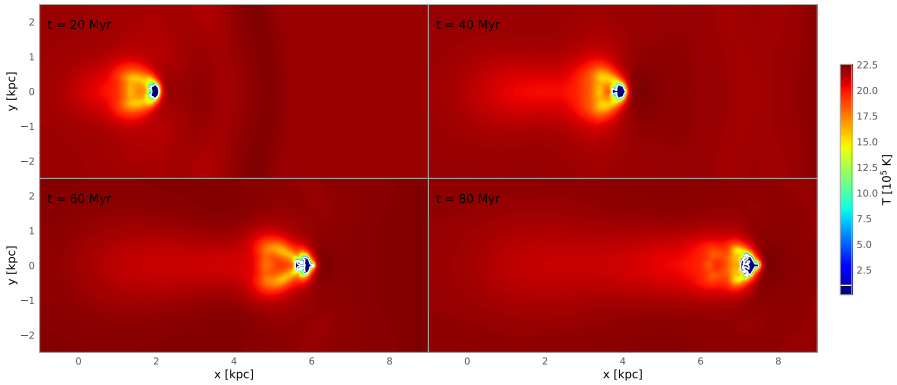

Figure 21: Same as Figure 8 for sim. 10 in Table 1.

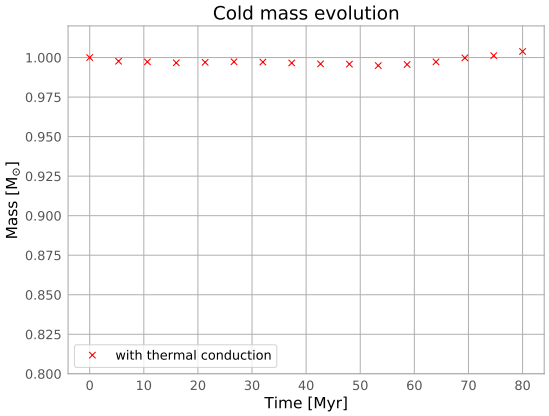

Figure 22: Results of sim. 10 in Table 1 for the cold mass evolution.

4.3 Survival of the cloud

We found from our simulations that at a distance of 100 kpc from the center, the mass losses are very low. Since at larger distances the coronal gas has even lower densities (see Figure 5), we expect very little interactions taking place between the corona and the cloud, and the mass losses should be negligible. We therefore calculate the survival time of the clouds starting from 100 kpc, assuming they did not lose any mass in the first part of the journey.

In order to obtain this time, we fitted the mass profiles shown in Figure 9, 12 and 14, and extrapolated the time needed for the clouds to lose all of their mass. This shows us that a cloud of 5×10^4 $M_\odot$ losses all of its mass after 2.9 Gyr without thermal conduction, and 3.6 Gyr with thermal conduction. For the low mass cloud (1×10^4 $M_\odot$), this is 2.5 Gyr (with thermal conduction) and 1.3 Gyr (without thermal conduction).

In order to understand whether our clouds can survive during their journey and accrete onto the galaxy disc, we compare this survival time with the infall time from 100 kpc to the galactic center, given as:

$$t_{fall} = \int_r^0 \frac{dr}{v(r)}, \tag{27}$$

where we start from $r = 100$ kpc and $v(r)$ is taken from the analytic velocity profile we calculated in Chapter 2 with equation (21).

For a cloud of mass $m_{cl} = 5 \times 10^4 M_\odot$ this is $t_{fall} = 0.55$ Gyr and for $m_{cl} = 1 \times 10^4 M_\odot$ the infall time is $t_{fall} = 0.70$ Gyr. As we already noticed from the velocity profile in Figure 6, we can exclude a difference in infall time due to different initial velocities, since both the two extreme cases converge towards each other at ~ 150 kpc from the disc.

Also taking into account the effect of gas condensation in the most inner regions of the CGM (Section 4.2), we should conclude that the gas is able to survive its way to the galactic disc, since the survival time of these clouds seems to be much larger than the time they need to reach the center. This means that the cold CGM clouds observed in the halos of spiral galaxies could be a viable way to accrete gas onto star-forming discs and therefore feed their star formation. However, we should caution that extrapolating the behaviour of the simulations in this way gives a rather uncertain estimate as non-linear effects can suddenly accelerate the destruction of the cloud. Simulations carried out for a much longer time would be needed to draw a firm conclusion.

5 Conclusions

In this Thesis, we have investigated the scenario in which the cold circumgalactic gas of a Milky Way-like spiral galaxy is composed of different clouds originating form the IGM that are infalling towards the galactic center and are interacting with the hot corona. The properties of both the hot and cold gas phases have been analytically estimated in order to be consistent with observational constraints (e.g. Tumlinson et al., 2013[44]; Werk et al., 2014[49]; Anderson & Bregman, 2011[2]). We performed high-resolution 2D hydrodynamical simulations to investigate the motion of the cold clouds through the hot ambient medium, focusing in particular on the influence of thermal conduction on the cloud survival time.

The main results and conclusions that we have obtained with this work are the following:

1. The main effect of thermal conduction in our simulations is its ability to keep the clouds compact during their motion through the corona. In Chapter 3 we have seen this effect in the development of the turbulent wake behind the cloud. The cold cloudlets present in the simulations with only cooling are instead suppressed in the simulations with thermal conduction, leaving a compact cloud traveling through the hot CGM. The survival time of the clouds for these two types of simulations are however comparable with each other.

2. Our simulations show how clouds of masses of the order of 10^4 $M_\odot$ have survival times that exceed the analytic predicted infall times considerably and therefore are able to survive their journey through the galaxy halos. We have also have found evidence for gas condensation in the central regions, which contributes to the survival as well. This finding is in agreement with what is found in the work of Armillotta et al. (2016[3]).

3. Given the previous results, we conclude that the observed cold CGM clouds, in the scenario in which they originate from the IGM, are a viable way to accrete gas onto the star-forming discs and therefore deed their star formation.

Acknowledgements

With this I come to the end of my bachelor research project, an inspiring, exciting, fruitful, joyful and long 2,5 months. I would like to thank Filippo and Andrea.

Andrea, I enjoyed working with you! I am thankful for all your guidance and patience whenever I came with an endless stream of questions, you stayed positive the whole time. I have a lot of respect for your knowledge and energy to put through. Although we did this project during very uncommon and strange times, the discussions and meetings we had via Zoom or Skype were always very amusing and interesting; I enjoyed it very much! I wish you all the best during the rest of your PhD!

Filippo, your experience in and passion for the work you do is impressive. With the curiosity to find out and positivity that you transmit to others, you have encouraged me throughout this whole project. I have learned a lot from you during the last semester.

Although in no way the knowledge and experience I gained during this journey is comparable with that of the both of you, I have learned a lot from the experience of the teamwork, passion, fascination and curiosity you both share. I am thankful to have been a small part of that.

References

[1] Andrea Afruni, Filippo Fraternali, and Gabriele Pezzulli. Cool circumgalactic gas of passive galaxies from cosmological inflow. , 625:A11, May 2019.

[2] Michael E. Anderson and Joel N. Bregman. Detection of a Hot Gaseous Halo around the Giant Spiral Galaxy NGC 1961. , 737(1):22, August 2011.

[3] L. Armillotta, F. Fraternali, and F. Marinacci. Efficiency of gas cooling and accretion at the disc-corona interface. , 462(4):4157–4170, November 2016.

[4] L. Armillotta, F. Fraternali, J. K. Werk, J. X. Prochaska, and F. Marinacci. The survival of gas clouds in the circumgalactic medium of Milky Way-like galaxies. , 470(1):114–125, September 2017.

[5] L. Armillotta, F. Fraternalli, J. K. Werk, J. X. Prochaska, and F. Marinacci. The survival of gas clouds in the Circumgalactic Medium of Milky Way-like galaxies. 2017.

[6] Armillotta, L. and Fraternalli, F. and Marinacci, F. Efficiency of gas cooling and accretion at the disc-corona interface. 2016.

[7] Michael Aumer and James J. Binney. Kinematics and history of the solar neighbourhood revisited. , 397(3):1286–1301, August 2009.

[8] James Binney. Modelling the Galaxy in the era of Gaia. *arXiv e-prints*, page arXiv:0911.2661, November 2009.

[9] Binney, J. and Nipoti, C. and Fraternalli, F. Do high-velocity clouds form by thermal instablility? 2009.

[10] Yuval Birnboim and Avishai Dekel. Virial shocks in galactic haloes? , 345(1):349–364, October 2003.

[11] Joel N. Bregman and Edward J. Lloyd-Davies. X-Ray Absorption from the Milky Way Halo and the Local Group. , 669(2):990–1002, November 2007.

[12] Greg L. Bryan and Michael L. Norman. Statistical Properties of X-Ray Clusters: Analytic and Numerical Comparisons. , 495(1):80–99, March 1998.

[13] Crighton, N. H. M. and Hennawi, J. F. and Prochaska, J. X. Metal-poor, Cool gas in the circumgalactic medium of a z=2.4 star-forming galaxy: direct evidence for cold accretion? 2013.

[14] C. R. Crowell and W. G. Spitzer. Attenuation length measurements of hot electrons and hot holes in metal films. *IEEE Transactions on Electron Devices*, 9(6):508–508, November 1962.

[15] Arianna Di Cintio, Chris B. Brook, Andrea V. Macciò, Greg S. Stinson, Alexander Knebe, Aaron A. Dutton, and James Wadsley. The dependence of dark matter profiles on the stellar-to-halo mass ratio: a prediction for cusps versus cores. , 437(1):415–423, January 2014.

[16] George B. Field. Thermal Instability. , 142:531, August 1965.

[17] F. Fraternali and J. J. Binney. Accretion of gas on to nearby spiral galaxies. , 386(2):935–944, May 2008.

[18] Filippo Fraternali. *Gas Accretion via Condensation and Fountains*, volume 430 of *Astrophysics and Space Science Library*, page 323. 2017.

[19] Gatto, A. and Fraternalli, F. and Read, J. I. and Marinacci, F. and Lux, H. and Walch, S. Unveilling the corona of the Milky Way via ram-pressure stripping of dwarf satellites. 2013.

[20] Timothy M. Heckman, Rachel M. Alexandroff, Sanchayeeta Borthakur, Roderik Overzier, and Claus Leitherer. The Systematic Properties of the Warm Phase of Starburst-Driven Galactic Winds. , 809(2):147, August 2015.

[21] M. Ryan Joung, Mary E. Putman, Greg L. Bryan, Ximena Fernández, and J. E. G. Peek. Gas Accretion is Dominated by Warm Ionized Gas in Milky Way Mass Galaxies at z ~0. , 759(2):137, November 2012.

[22] Brian A. Keeney, John T. Stocke, Charles W. Danforth, J. Michael Shull, Cameron T. Pratt, Cynthia S. Froning, James C. Green, Steven V. Penton, and Blair D. Savage. Characterizing the Circumgalactic Medium of Nearby Galaxies with HST/COS and HST/STIS Absorption-line Spectroscopy. II. Methods and Models. , 230(1):6, May 2017.

[23] Jr. Kennicutt, R. C. and S. M. Kent. A survey of H-alpha emission in normal galaxies. , 88:1094–1107, August 1983.

[24] Ethan Kruse, J. Tumlinson, C. Thom, and K. Sembach. COS Observations of Molecular H_2 at z = 0.248. In *American Astronomical Society Meeting Abstracts #217*, volume 217 of *American Astronomical Society Meeting Abstracts*, page 335.09, January 2011.

[25] D. Lecoanet, M. McCourt, E. Quataert, K. J. Burns, G. M. Vasil, J. S. Oishi, B. P. Brown, J. M. Stone, and R. M. O'Leary. A validated non-linear Kelvin-Helmholtz benchmark for numerical hydrodynamics. , 455(4):4274–4288, February 2016.

[26] Ariyeh H. Maller and James S. Bullock. Multiphase galaxy formation: high-velocity clouds and the missing baryon problem. , 355(3):694–712, December 2004.

[27] A. Marasco and F. Fraternali. Modelling the H I halo of the Milky Way. , 525:A134, January 2011.

[28] Federico Marinacci, James Binney, Filippo Fraternali, Carlo Nipoti, Luca Ciotti, and Pasquale Londrillo. The mode of gas accretion on to star-forming galaxies. , 404(3):1464–1474, May 2010.

[29] Federico Marinacci, Filippo Fraternali, Carlo Nipoti, James Binney, Luca Ciotti, and Pasquale Londrillo. Galactic fountains and the rotation of disc-galaxy coronae. , 415(2):1534–1542, August 2011.

[30] Stacy S. McGaugh and Joe Wolf. Local Group Dwarf Spheroidals: Correlated Deviations from the Baryonic Tully-Fisher Relation. , 722(1):248–261, October 2010.

[31] Matthew J. Miller and Joel N. Bregman. Constraining the Milky Way's Hot Gas Halo with O VII and O VIII Emission Lines. , 800(1):14, February 2015.

[32] Julio F. Navarro, Carlos S. Frenk, and Simon D. M. White. The Structure of Cold Dark Matter Halos. , 462:563, May 1996.

[33] Lorenzo Posti, Filippo Fraternali, and Antonino Marasco. Peak star formation efficiency and no missing baryons in massive spirals. , 626:A56, June 2019.

[34] M. E. Putman, J. E. G. Peek, and M. R. Joung. Gaseous Galaxy Halos. , 50:491–529, September 2012.

[35] M. E. Putman, D. R. Saul, and E. Mets. Head-tail clouds: drops to probe the diffuse Galactic halo. , 418(3):1575–1586, December 2011.

[36] A. B. Rechester and M. N. Rosenbluth. Electron heat transport in a tokamak with destroyed magnetic surfaces. , 40(1):38–41, January 1978.

[37] Renzo Sancisi, Filippo Fraternali, Tom Oosterloo, and Thijs van der Hulst. Cold gas accretion in galaxies. , 15(3):189–223, June 2008.

[38] K. R. Sembach, B. P. Wakker, B. D. Savage, P. Richter, M. Meade, J. M. Shull, E. B. Jenkins, G. Sonneborn, and H. W. Moos. Highly Ionized High-Velocity Gas in the Vicinity of the Galaxy. , 146(1):165–208, May 2003.

[39] Shull, J. M. Where do galaxies end? 2014.

[40] Jr. Spitzer, Lyman. On a Possible Interstellar Galactic Corona. , 124:20, July 1956.

[41] James M. Stone, Thomas A. Gardiner, Peter Teuben, John F. Hawley, and Jacob B. Simon. Athena: A New Code for Astrophysical MHD. , 178(1):137–177, September 2008.

[42] Ralph S. Sutherland and M. A. Dopita. Cooling Functions for Low-Density Astrophysical Plasmas. , 88:253, September 1993.

[43] Christopher Thom, Jason Tumlinson, Jessica K. Werk, J. Xavier Prochaska, Benjamin D. Oppenheimer, Molly S. Peeples, Todd M. Tripp, Neal S. Katz, John M. O'Meara, Amanda Brady Ford, Romeel Davé, Kenneth R. Sembach, and David H. Weinberg. Not Dead Yet: Cool Circumgalactic Gas in the Halos of Early-type Galaxies. , 758(2):L41, October 2012.

[44] Jason Tumlinson, Christopher Thom, Jessica K. Werk, J. Xavier Prochaska, Todd M. Tripp, Neal Katz, Romeel Davé, Benjamin D. Oppenheimer, Joseph D. Meiring, Amanda Brady Ford, John M. O'Meara, Molly S. Peeples, Kenneth R. Sembach, and David H. Weinberg. The COS-Halos Survey: Rationale, Design, and a Census of Circumgalactic Neutral Hydrogen. , 777(1):59, November 2013.

[45] B. P. Wakker. Distances and Metallicities of High- and Intermediate-Velocity Clouds. , 136(2):463–535, October 2001.

[46] B. P. Wakker and H. van Woerden. Distribution and origin of high-velocity clouds. III. Clouds, complexes and populations. , 250:509–532, October 1991.

[47] B. P. Wakker and H. van Woerden. High-Velocity Clouds. , 35:217–266, January 1997.

[48] B. P. Wakker, D. G. York, J. C. Howk, J. C. Barentine, R. Wilhelm, R. F. Peletier, H. van Woerden, T. C. Beers, Ž. Ivezić, P. Richter, and U. J. Schwarz. Distances to Galactic High-Velocity Clouds: Complex C. , 670(2):L113–L116, December 2007.

[49] Jessica K. Werk, J. Xavier Prochaska, Jason Tumlinson, Molly S. Peeples, Todd M. Tripp, Andrew J. Fox, Nicolas Lehner, Christopher Thom, John M. O'Meara, Amanda Brady Ford, Rongmon Bordoloi, Neal Katz, Nicolas Tejos, Benjamin D. Oppenheimer, Romeel Davé, and David H. Weinberg. The COS-Halos Survey: Physical Conditions and Baryonic Mass in the Low-redshift Circumgalactic Medium. , 792(1):8, September 2014.

[50] Simon D. M. White and Carlos S. Frenk. Galaxy Formation through Hierarchical Clustering. , 379:52, September 1991.

[51] Fakhri S. Zahedy, Hsiao-Wen Chen, Sean D. Johnson, Rebecca M. Pierce, Michael Rauch, Yun-Hsin Huang, Benjamin J. Weiner, and Jean-René Gauthier. Characterizing circumgalactic gas around massive ellipticals at z $\sim$ 0.4 - II. Physical properties and elemental abundances. , 484(2):2257–2280, April 2019.